

Article

Cerium Niobate Hollow Sphere Engineered Graphitic Carbon Nitride for Synergistic Photothermal/Chemodynamic Cancer Therapy

Kayalvizhi Samuvel Muthiah¹, Senthilkumar Thirumurugan¹, Yu-Chien Lin¹, Rajalakshmi Sakthivel¹, Udesh Dhawan² , An-Ni Wang³ , Michael Hsiao^{4,5}  and Ren-Jei Chung^{1,6,*} 

¹ Department of Chemical Engineering and Biotechnology, National Taipei University of Technology (Taipei Tech), Taipei 106, Taiwan; get2kayal35@gmail.com (K.S.M.); senthilkumar2595@gmail.com (S.T.); yuchien.lin91@gmail.com (Y.-C.L.); rajalakshmicnr@gmail.com (R.S.)

² Centre for the Cellular Microenvironment, Division of Biomedical Engineering, James Watt School of Engineering, Mazumdar-Shaw Advanced Research Centre, University of Glasgow, Glasgow G116EW, UK; udesh.dhawan@glasgow.ac.uk

³ Scrona AG, Grubenstrasse 9, 8045 Zürich, Switzerland; anni.wang@scrona.com

⁴ Genomics Research Center, Academia Sinica, Taipei 115, Taiwan; mhsiao@gate.sinica.edu.tw

⁵ Department of Biochemistry, College of Medicine, Kaohsiung Medical University, Kaohsiung 807, Taiwan

⁶ High-Value Biomaterials Research and Commercialization Center, National Taipei University of Technology (Taipei Tech), Taipei 10608, Taiwan

* Correspondence: rjchung@mail.ntut.edu.tw; Tel.: +886-2-2771-2171 (ext. 2547)

Abstract: Reactive oxygen species (ROS)-mediated chemodynamic therapy (CDT) and photothermal therapy (PTT) have potential for various cancer treatments. However, they are still bound by the demands of Fenton reaction conditions such as oxygen dependence, inherent defects in common standard photosensitizers (PSs), and the continuous availability of laser sources. Herein, we designed Ce₃NbO₇/g-C₃N₄ nanocomposites (NCs) and investigated their ability to evaluate the performance of PTT/CDT synergistically to enhance cancer treatment. The activation of Ce₃NbO₇/g-C₃N₄ NCs in the tumor microenvironment (TME) causes the generation of cytotoxic ROS via the Fenton reaction. Additionally, the g-C₃N₄ in NCs absorbs NIR, generating hyperthermia in the TME. The photothermal conversion efficiency (η) of the Ce₃NbO₇/g-C₃N₄ NCs was found to be 49.5%. A photocatalytic reaction with PTT-enhanced Fenton reagents, without consuming additional photothermal agents (PTA) or Fenton reagents, generates the hydroxyl radical (OH•) primarily by direct electron transfer in the TME. Almost 68% of cells experienced programmed cell death due to the combinational effect (PTT/CDT), making it an efficient and biocompatible therapy. Furthermore, this work provides a basis for developing numerous innovative materials that can be used to treat cancer, overcome general limitations, and enhance ROS production under single-wavelength (808 nm) laser irradiation.

Keywords: chemodynamic therapy; photothermal therapy; tumor microenvironment; Fenton reaction



Citation: Muthiah, K.S.; Thirumurugan, S.; Lin, Y.-C.; Sakthivel, R.; Dhawan, U.; Wang, A.-N.; Hsiao, M.; Chung, R.-J. Cerium Niobate Hollow Sphere Engineered Graphitic Carbon Nitride for Synergistic Photothermal/Chemodynamic Cancer Therapy. *Crystals* **2023**, *13*, 954. <https://doi.org/10.3390/cryst13060954>

Academic Editor: Marian Valko

Received: 18 May 2023

Revised: 10 June 2023

Accepted: 12 June 2023

Published: 15 June 2023



Copyright: © 2023 by the authors. Licensee MDPI, Basel, Switzerland. This article is an open access article distributed under the terms and conditions of the Creative Commons Attribution (CC BY) license (<https://creativecommons.org/licenses/by/4.0/>).

1. Introduction

Cancer has the highest mortality rate, accounting for 9.6 million deaths globally in 2018 [1,2]. According to the World Health Organization (WHO), nearly 35% of cancer deaths occur due to changes in lifestyles (including smoking and alcohol consumption), dietary factors, and exposure to ultraviolet rays and ionizing radiation [3–6]. Hepatitis B and C viruses, fatty liver disease, cirrhosis brought on by alcohol use, smoking, obesity, diabetes, an excess of iron in the diet, and other dietary exposures are the risk factors for liver cancer (LC) [7]. LC is one of the most common cancers [8,9] and ranks third in mortality rate among all malignancies, with an estimated 830,130 deaths globally in 2020 [10–12]. Worldwide, LC is the leading form of cancer [9,13]. The WHO estimates around 905,677 new cases annually and reports that 1,276,679 people will die from LC in 2040 [10,14]. Several traditional cancer

treatments, including surgery, radiation therapy, and chemotherapy, have been widely used; however, all these therapies are “double-edged swords” due to their high rates of recurrence, harsh side effects, and multidrug resistance [15]. Therefore, there is a need to develop a novel methodology for attaining more efficacy with negligible side effects [16–20], such as sonodynamic therapy (SDT) [18], photodynamic therapy (PDT) [19], chemodynamic therapy (CDT) [20], and photothermal ablation therapy (PAT) [17,19]. A nanocatalytic medicine is an emerging therapeutic concept, producing toxic ROS that actively targets the tumor tissues without harming the normal tissues [21]. The tumor microenvironment (TME) is mildly acidic and hypoxic, expressing H_2O_2 , promoting tumor growth and spread. Therefore, the creation of nanoplateforms for TME-responsive tumor therapy appears to be promising. CDT is the most widely used approach in nanocatalytic medicine and is wholly based on biological characteristics linking various metabolic pathways between tumor cells and normal cells. These biological qualities can produce distinctive biochemical conditions, such as moderate acidity and abundant H_2O_2 , to stimulate specific chemical reactions, particularly the Fenton/Fenton-like reaction within tumors. These interactions produce the highly toxic hydroxyl radical ($\text{OH}\bullet$), which causes tissue damage and tumor cell death. The produced $\text{OH}\bullet$ induces primary tumor death in TME, causing these tumor cells to produce tumor-associated antigens (TAAs). The TAAs are captured by dendritic cells (DCs) and migrate to immune organs such as the spleen [22,23]. Some of the metals involved in CDT are Fe [24,25], Mn [26,27], Co [28,29], Ag [30,31], and Cu [32,33]. Recently, a new class of bio-antioxidants called cerium-oxide-based nanozymes has been developed [34,35]. In nature, cerium has two different oxidation states, Ce^{3+} and Ce^{4+} , and the enzymatic activity of $\text{CeO}_2\text{-x}$ scavenging ROS is assumed to be related to the self-regeneration cycle of $\text{Ce}^{3+}/\text{Ce}^{4+}$ and the oxygen vacancies on the cerium oxide surface. Most researchers believe $\text{Ce}^{3+}/\text{Ce}^{4+}$ redox cycling is directly associated with $\text{CeO}_2\text{-xs}$ antioxidant properties. The potential significance of oxygen vacancies in the rapid redox cycling of $\text{CeO}_2\text{-x}$ is still under discussion [2,35,36]. Herein, we constructed cerium niobate hollow spheres ($\text{CeO}_2/\text{Ce}_3\text{NbO}_7/\text{g-C}_3\text{N}_4$ NCs), where Ce_3NbO_7 is meant for CDT purposes.

Owing to its inherent noninvasiveness and negligible side effects, photothermal therapy (PTT) is widely used in cancer therapy. It uses photothermal agents (PTAs) that convert light energy into thermal energy to generate localized hyperthermia; this has been considered an alternative treatment for various cancers [19,37]. Graphitic polymeric carbon nitride ($\text{g-C}_3\text{N}_4$) has gained attention as a novel material that resembles graphene due to its distinct elemental makeup and photoelectric properties. The exceptional biocompatibility of $\text{g-C}_3\text{N}_4$, a compound made exclusively of carbon and nitrogen, is advantageous for use in biomedicine [38]. Due to its superior physical and chemical characteristics, such as ease of preparation, stable fluorescence, appropriate energy level, a wide excitation wavelength range, and high biocompatibility, $\text{g-C}_3\text{N}_4$ is an emerging polymeric material with excellent performance in PTT and photocatalyst applications. However, evidence on its application as a biomedicine is scarce [39].

In this work, we designed NCs composed of cerium niobate ($\text{CeO}_2/\text{Ce}_3\text{NbO}_7$) hollow spheres coated with $\text{g-C}_3\text{N}_4$ nanosheets ($\text{Ce}_3\text{NbO}_7/\text{g-C}_3\text{N}_4$ NCs) with excellent biocompatibility, enhancing both CDT and PTT for synergistically killing tumor cells. The overall scheme of the work is given in Figure 1. The designed $\text{Ce}_3\text{NbO}_7/\text{g-C}_3\text{N}_4$ NCs possess the Ce^{3+} ions that actively take part in the Fenton reaction via the cascade mechanism to yield the $\text{OH}\bullet$ radical; the $\text{g-C}_3\text{N}_4$ nanosheets to the hollow spheres act as excellent PTA agents and exhibit an outstanding photothermal conversion efficiency (η) of 49.5% due to higher carbon content. Notably, the synthesized NCs feature an “all in one” therapeutic platform for performing both PTT/CDT without adding any external photothermal or chemodynamic (Fenton) agents. Hence, our synthesized NCs show a novel approach for accessible design and hold great potential in therapeutic applications. Integrating PTT/CDT significantly improves the progression of cell apoptosis by enhancing one mode of therapy with the other through synergistic performance by heat generation in PTT and the production of

OH• in CDT. The excellent synergistic performance of the in vitro results of both PTT and CDT illustrates the potential of NCs as a cancer-curing treatment technique.

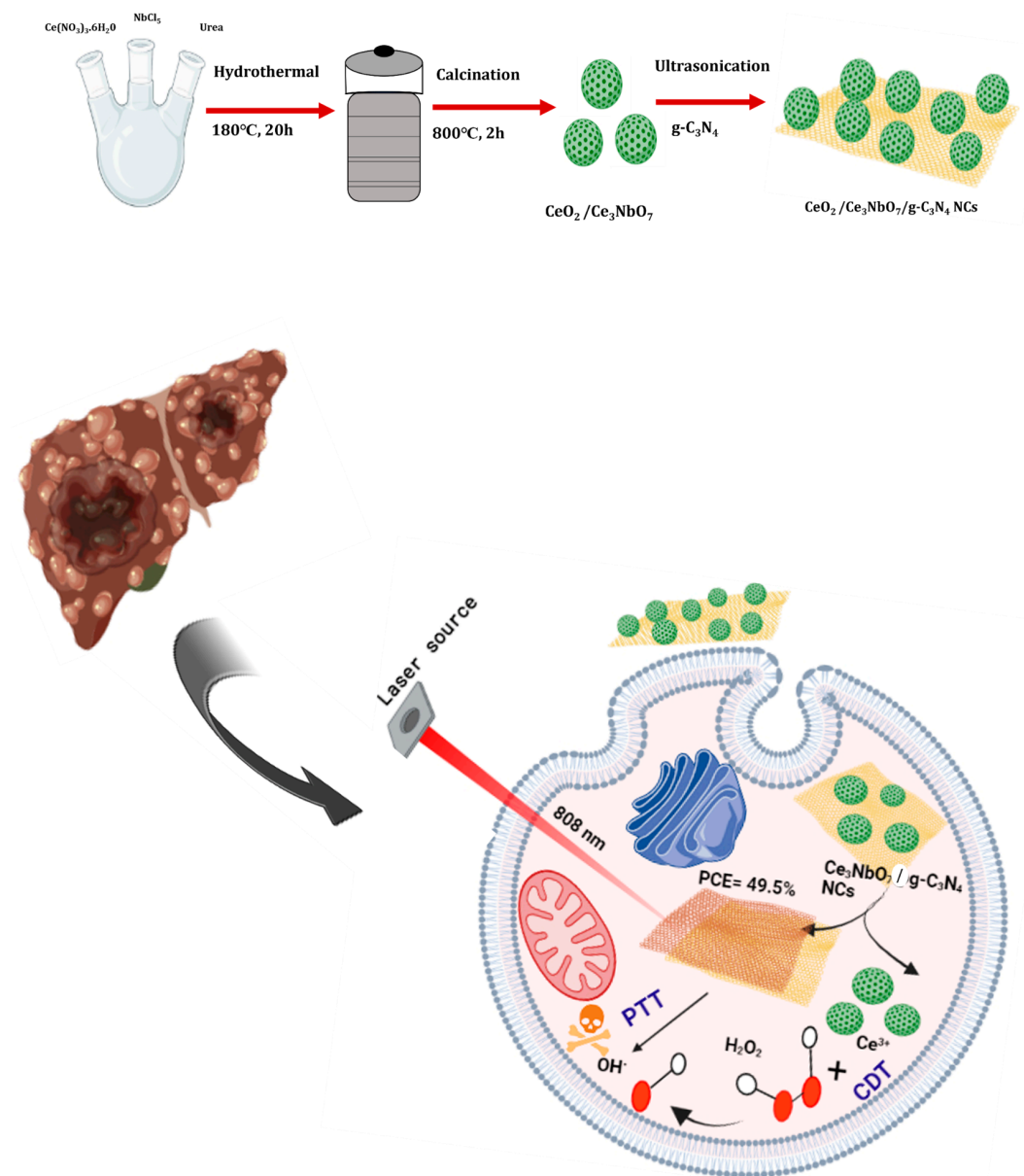


Figure 1. Schematic representation of the synthesis and therapeutic application of the $\text{CeO}_2/\text{Ce}_3\text{NbO}_7/\text{g-C}_3\text{N}_4$ NCs. The modifications of $\text{g-C}_3\text{N}_4$ to the Ce_3NbO_7 hollow spheres synergistically accomplish PTT/CDT to treat LC.

2. Materials and Methods

2.1. Required Chemicals

A total of 99.5% cerium nitrate hexahydrate ($\text{Ce}(\text{NO}_3)_3 \cdot 6\text{H}_2\text{O}$), 99.9% niobium pentachloride (NbCl_5), 99% urea ($\text{CH}_4\text{N}_2\text{O}$), 35% hydrogen peroxide (H_2O_2), 99% ethanol ($\text{C}_6\text{H}_5\text{OH}$), graphitic carbon nitride ($\text{g-C}_3\text{N}_4$), double distilled water (DD H_2O), dimethyl sulfoxide (DMSO), 3-(4,5-dimethylthiazol-2-yl)-2,5-diphenyl tetrazolium bromide (MTT), and methylene blue (MB) were purchased from Sigma-Aldrich, Burlington, MA, USA, or Merck, Darmstadt, Germany.

2.2. Preparation for CeO₂/Ce₃NbO₇ Hollow Spheres

The CeO₂/Ce₃NbO₇ were prepared by the facile hydrothermal method. Initially, about 0.303 g of cerium nitrate hexahydrate (Ce(NO₃)₃·6H₂O) and 0.18 g of niobium pentachloride (NbCl₅) were dissolved in 70 mL of DD H₂O. In the above solution, 1 g of urea (CH₄N₂O) was added dropwise with constant stirring. Then, 4–5 drops of H₂O₂ were added; the mixture was kept on a magnetic stirrer for 1 h. The clear solution was transferred to a Teflon-lined autoclave and sealed. The above solution was subjected to a hydrothermal process at 180 °C for 20 h. The pale green precipitate obtained was washed four times with ethanol and DD H₂O and dried in an oven at 60 °C for 15 h. After drying, the sample was calcined at 800 °C for 2 h. The resultant black powder was stored and labeled as cerium niobate hollow spheres.

2.3. Preparation of g-C₃N₄

The g-C₃N₄ was prepared by using the pyrolysis method. Initially, 20 mg of CH₄N₂O was placed in a crucible and subjected to pyrolysis at 550 °C for 3 h.

2.4. Modification of g-C₃N₄ on CeO₂/Ce₃NbO₇ Hollow Spheres

The CeO₂/Ce₃NbO₇/g-C₃N₄ NCs were prepared by coating the CeO₂/Ce₃NbO₇ hollow spheres on the surface of g-C₃N₄ nanosheets by the ultrasonication method. The calculated amounts of the CeO₂/Ce₃NbO₇ hollow spheres and g-C₃N₄ were taken in the molar ratio of 1:4 by weight (20% of CeO₂/Ce₃NbO₇ hollow spheres and 80% of g-C₃N₄). The desired amount of CeO₂/Ce₃NbO₇ hollow spheres was dissolved in ethanol, followed by the addition of g-C₃N₄ nanosheets during ultrasonication for 10 min, and the residue was dried in an oven at 60 °C overnight. Later, the dried mixture of CeO₂/Ce₃NbO₇/g-C₃N₄ was placed in a boat-shaped crucible and set in a muffle furnace at 550 °C with a heating ramp rate of 10 °C /min in an argon atmosphere for 4 h. Finally, the obtained CeO₂/Ce₃NbO₇/g-C₃N₄ NCs were dried and ground into powder.

2.5. Characterization of Synthesized g-C₃N₄-Coated NCs

The morphological examination of CeO₂/Ce₃NbO₇ hollow spheres and CeO₂/Ce₃NbO₇/g-C₃N₄ NCs was determined by transmission electron microscopy (TEM). The crystallinity of the g-C₃N₄-coated NCs was confirmed by X-ray diffraction spectroscopy (XRD), and their surface conformation was predicted by energy-dispersive X-ray spectroscopy (EDS). The stretching of various vibrational bands and the presence of different functional groups were indicated using Fourier transform infrared spectroscopy (FT-IR). The elemental composition and orbital range of the synthesized NCs were determined by X-ray photoelectron spectroscopy (XPS), and their photothermal response was determined using an infrared (IR) camera. The respective cell viability and biocompatibility of the NCs were monitored by MTT assay.

2.6. Photothermal Response of the Synthesized CeO₂/Ce₃NbO₇/g-C₃N₄ NCs

The time-dependent temperature profiles of the CeO₂/Ce₃NbO₇/g-C₃N₄ NCs were assessed at an irradiation of 808 nm using a near-infrared (NIR) laser. The images were obtained using the infrared (IR) camera. The synthesized CeO₂/Ce₃NbO₇/g-C₃N₄ NCs were dissolved in 1 mL of DD H₂O at different concentrations (0.1, 0.2, 0.5, 1, and 2 mg/mL), placed in a 2 mL cuvette, and subjected to laser exposure at 1 W/cm² for 5 min. The thermal images and temperature elevation of the synthesized NCs concerning different concentrations and their cooling curves were recorded using an IR camera. The photothermal conversion efficiency (η) was calculated using the formula given below:

$$\eta = \frac{hs(T_{\max} - T_{\text{surr}}) - Q_{\text{dis}}}{I(1 - 10^{-A_{808}})} \quad (1)$$

where h = heat transfer coefficient, S = superficial area, T_{\max} = maximum equilibrium temperature, T_{sur} = ambient surrounding temperature, Q_{dis} = heat dissipated by the surrounding, I = laser power, and A_{808} = absorbance of the NCs at 808 nm.

2.7. Cell Culture

Human liver cancer HepG-2 cells (ATCC-CCL107, Manassas, VA, USA) and mouse fibroblasts L929 cells (ATCC-CCL1, Manassas, VA, USA) were cultured in Dulbecco's modified Eagle's medium (DMEM) with 10% fetal bovine serum (GIBCO, Ann Arbor, MI, USA), 100 $\mu\text{g}/\text{mL}$ of penicillin, and 100 $\mu\text{g}/\text{mL}$ of streptomycin. The incubators were maintained at 37 °C with a 5% CO_2 atmosphere and 95% relative humidity.

2.8. OH• Generation of $\text{CeO}_2/\text{Ce}_3\text{NbO}_7/\text{g-C}_3\text{N}_4$ NCs by MB

Initially, 0.2 mg of the $\text{CeO}_2/\text{Ce}_3\text{NbO}_7/\text{g-C}_3\text{N}_4$ NCs were added to 10 μL of H_2O_2 and 1 mL of MB solution (10 μM). After incubation for approximately 20 min at room temperature, this solution was subjected to UV spectrometry, and its absorbance was measured at 660 nm.

2.9. In Vitro Cytotoxicity Assay

To evaluate the biocompatibility of the prepared $\text{CeO}_2/\text{Ce}_3\text{NbO}_7/\text{g-C}_3\text{N}_4$ NCs, $5 \times 10^4/\text{mL}$ of both L929 and HepG-2 cells were seeded in a 96-well plate, cultured and kept in an oven at 37 °C with 5% of CO_2 for 12 h. Later, the DMEM medium was removed, and fresh DMEM containing different concentrations of NCs (0, 12.5, 25, 50, and 100 $\mu\text{g}/\text{mL}$) was added to a 96-well plate and incubated for 24 h. The medium in the 96-well plate was removed the following day, and MTT solution (100 μL) was added and incubated for 3 h. Then, the MTT solution was discarded and DMSO solution was added to the 96-well plate; this was shaken well at 100 rpm for 20 min, and absorbance at 570 nm was measured using a Varioscan[®] flash microplate reader (Thermo Scientific, Waltham, MA, USA).

In the cytotoxicity analysis, 5×10^4 HepG-2 cells were seeded in a 96-well plate with different groups such as control (DMEM medium), $\text{CeO}_2/\text{Ce}_3\text{NbO}_7/\text{g-C}_3\text{N}_4$ NCs, and $\text{CeO}_2/\text{Ce}_3\text{NbO}_7/\text{g-C}_3\text{N}_4$ NCs + NIR (808 nm laser source) at two different pH (7.4 and 6.5) to mimic TME. Finally, the cell viability was determined using the MTT assay.

2.10. Statistical Analysis

All the obtained data in the present work are represented as mean \pm standard deviation. Significance between the groups was calculated using the Student's t -test method. A p -value less than 0.5 was considered to be statistically significant.

3. Results and Discussion

3.1. Synthesis and Characterization of $\text{CeO}_2/\text{Ce}_3\text{NbO}_7/\text{g-C}_3\text{N}_4$ NCs

Using the facile hydrothermal method, the $\text{CeO}_2/\text{Ce}_3\text{NbO}_7$ hollow spheres were prepared [40], and their $\text{g-C}_3\text{N}_4$ synthesis was performed using the pyrolysis method [41]. The surface modification of $\text{g-C}_3\text{N}_4$ towards the $\text{CeO}_2/\text{Ce}_3\text{NbO}_7$ hollow spheres via the ultrasonication method is given in Figure 1.

Figure 2a,b shows the structure of the prepared $\text{CeO}_2/\text{Ce}_3\text{NbO}_7$ hollow spheres. TEM images of $\text{g-C}_3\text{N}_4$ show a nanosheet-like structure (Figure 2c,d), and Figure 2e,f shows the hollow-sphere-shape of the $\text{CeO}_2/\text{Ce}_3\text{NbO}_7/\text{g-C}_3\text{N}_4$ NCs that were modified on the surface of the $\text{g-C}_3\text{N}_4$ nanosheets. Herein, the sphere-shaped structures of $\text{CeO}_2/\text{Ce}_3\text{NbO}_7$ were produced during the calcination process (800 °C for 2 h). The EDX spectrum revealed the elemental constitution and weight percentage of the NCs. Figure 2g represents the EDX mapping of the $\text{CeO}_2/\text{Ce}_3\text{NbO}_7/\text{g-C}_3\text{N}_4$ NCs and confirms the presence of all elements such as cerium (Ce), niobium (Nb), oxygen (O), carbon (C), and nitrogen (N). Various colors in the signal indicated the presence of these components. Figure 2h presents the EDX images of Ce, while those of Nb (2i), C (2j), N (2k), and O (2l), respectively, are also provided. Numerous bright electron diffraction spots confirm the crystalline structure of

$\text{CeO}_2/\text{Ce}_3\text{NbO}_7/\text{g-C}_3\text{N}_4$ NCs. The EDX analysis was performed to elucidate the existence of elements such as Ce, Nb, C, N, and O in the prepared $\text{CeO}_2/\text{Ce}_3\text{NbO}_7/\text{g-C}_3\text{N}_4$ NCs. Figure 2m represents the EDX mapping of the respective NCs. Figure 2n shows the weight percentage and the elemental composition of the NCs, where the elements Ce, Nb, C, N, and O were present at 34.33, 47.05, 5.23, 12.91, and 0.47 wt%, respectively.

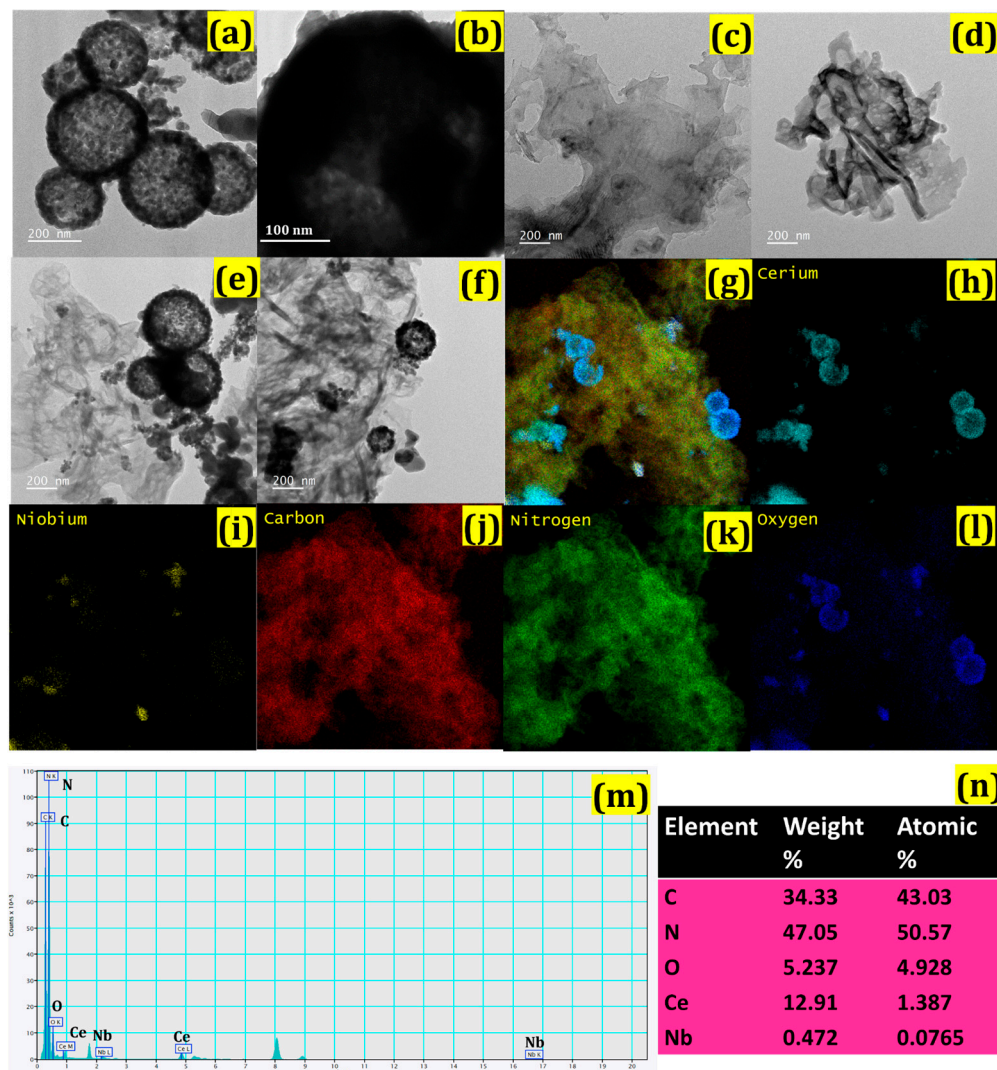


Figure 2. Characterization of $\text{CeO}_2/\text{Ce}_3\text{NbO}_7/\text{g-C}_3\text{N}_4$ NCs, (a,b) show TEM images of $\text{CeO}_2/\text{Ce}_3\text{NbO}_7$ hollow spheres; (c,d) $\text{g-C}_3\text{N}_4$; (e,f) $\text{CeO}_2/\text{Ce}_3\text{NbO}_7/\text{g-C}_3\text{N}_4$ NCs; (g) elemental mapping images of $\text{CeO}_2/\text{Ce}_3\text{NbO}_7/\text{g-C}_3\text{N}_4$ NCs; (h) cerium (Ce); (i) niobium (Nb); (j) carbon (C); (k) nitrogen (N); (l) oxygen (O); (m) EDX mapping of $\text{CeO}_2/\text{Ce}_3\text{NbO}_7/\text{g-C}_3\text{N}_4$ NCs; (n) elemental composition and weight percentage.

The XRD patterns of Ce_3NbO_7 , $\text{g-C}_3\text{N}_4$, and $\text{CeO}_2/\text{Ce}_3\text{NbO}_7/\text{g-C}_3\text{N}_4$ NCs are given in Figure 3a. The XRD pattern of $\text{CeO}_2/\text{Ce}_3\text{NbO}_7$ hollow spheres shows the characteristic peaks at 28.6 , 33.1 , 47.5 , 56.4 , 59.2 , and 69.5° , which correspond to the (111), (200), (220), (311), (222), and (400) planes of the cubic lattice of Ce_3NbO_7 [PDF No.: 00-023-0144], while the presence of tiny, intense peaks at 28 , 76.7 , and 79.1° correspond to the (111), (331), and (420) planes of CeO_2 , with a cubic structure [PDF No.: 00-001-0800] [42]. The XRD stick pattern of the composition of Ce_3NbO_7 [PDF No.: 00-023-0144] [43] confirms the composition of Ce and Nb in the $\text{CeO}_2/\text{Ce}_3\text{NbO}_7$ hollow spheres. The modification of $\text{g-C}_3\text{N}_4$ nanosheets towards $\text{CeO}_2/\text{Ce}_3\text{NbO}_7$ hollow spheres shows the presence of a characteristic peak at 27.5° , corresponding to the (001) coordinates confirming the presence

of $g\text{-C}_3\text{N}_4$ in the synthesized $\text{CeO}_2/\text{Ce}_3\text{NbO}_7/g\text{-C}_3\text{N}_4$ NCs [41]. Thus, XRD analysis confirmed that the $g\text{-C}_3\text{N}_4$ was successfully modified on $\text{CeO}_2/\text{Ce}_3\text{NbO}_7$ hollow spheres. The functional groups and structural moieties of the NCs were determined by FT-IR spectroscopy. Figure 3b represents the FT-IR spectrum of the NCs, with peaks at 605, 926, 1633, 2848, and 2919 cm^{-1} . The peaks in the 605 and 926 cm^{-1} region strongly convey Ce-O and Nb-O stretching vibrational modes. The C=O groups, -C-H- stretching, and hydroxy -OH groups were attributed to the presence of peaks at 1633, 2848, and 2919 cm^{-1} [40]. The appearance of a peak in the 1600–1900 cm^{-1} range confirms the presence of aromatic C-N stretching mode, and the sharp characteristic peak at 806 cm^{-1} was due to the presence of the *s*-triazine ring system [41]. The UV-visible spectrum of the $\text{CeO}_2/\text{Ce}_3\text{NbO}_7$, $g\text{-C}_3\text{N}_4$, and $\text{CeO}_2/\text{Ce}_3\text{NbO}_7/g\text{-C}_3\text{N}_4$ NCs upon 808 nm of NIR laser irradiation is given in Figure 3c. It is clearly observed that $g\text{-C}_3\text{N}_4$ exhibits a significant absorption spectrum in the range of 300–500 nm. Moreover, it is confirmed that the up-converted UV and visible emissions from the $\text{CeO}_2/\text{Ce}_3\text{NbO}_7$ NPs activate the $g\text{-C}_3\text{N}_4$ nanosheets. Therefore, our NCs possess a broad band spectrum from the visible to Near IR region [44].

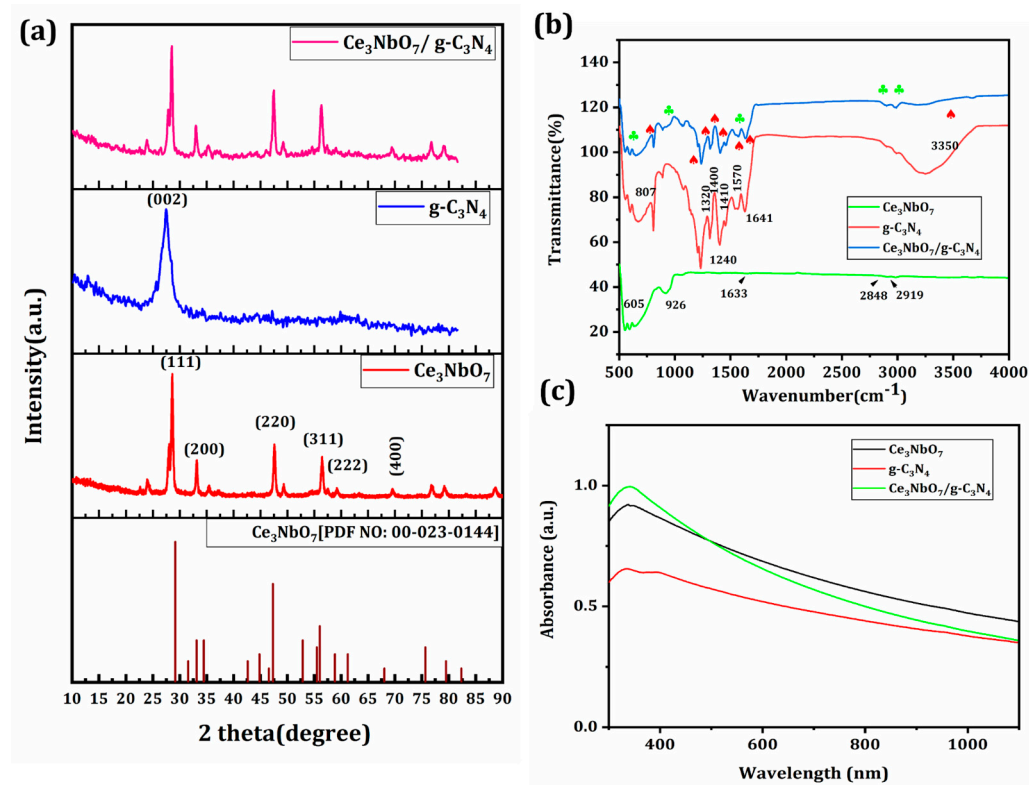


Figure 3. XRD patterns of $\text{CeO}_2/\text{Ce}_3\text{NbO}_7$, $g\text{-C}_3\text{N}_4$, and $\text{CeO}_2/\text{Ce}_3\text{NbO}_7/g\text{-C}_3\text{N}_4$ NCs (a); FT-IR spectra of $\text{CeO}_2/\text{Ce}_3\text{NbO}_7$, $g\text{-C}_3\text{N}_4$, and $\text{CeO}_2/\text{Ce}_3\text{NbO}_7/g\text{-C}_3\text{N}_4$ NCs (b), and (c) UV-visible spectrum of $\text{CeO}_2/\text{Ce}_3\text{NbO}_7$, $g\text{-C}_3\text{N}_4$, and $\text{CeO}_2/\text{Ce}_3\text{NbO}_7/g\text{-C}_3\text{N}_4$ NCs.

The XPS spectra of the constructed $\text{CeO}_2/\text{Ce}_3\text{NbO}_7/g\text{-C}_3\text{N}_4$ NCs are depicted in Figure 4, validating the presence of elements along with the structural behavior of NCs. Figure 4a shows the overall survey spectrum of $\text{CeO}_2/\text{Ce}_3\text{NbO}_7/g\text{-C}_3\text{N}_4$ NCs, confirming the existence of elements such as Ce, Nb, O, C, and N. This leads to the conformation of $\text{CeO}_2/\text{Ce}_3\text{NbO}_7$ modification towards the $g\text{-C}_3\text{N}_4$ in the NCs. Here, small, intense peaks at 283.8 eV (C1s) and 378.2 eV (N 1s) ($g\text{-C}_3\text{N}_4$) were obtained. Figure 4b depicts the deconvoluted spectra of Ce 3d $_{5/2}$ and Ce 3d $_{3/2}$, which show the appearance of six peaks attributed to the presence of Ce^{4+} and Ce^{3+} at 883.6 eV (v), 890.1 eV (v'), 899.4 eV (v''), 902 eV (u), 908.7 eV (u'), and 917.8 eV (u'') [45]. The presence of the Nb^{5+} oxidation state was confirmed by the appearance of the noticeable peaks at 208 eV (Nb 3d $_{5/2}$) and 211.1 eV (Nb 3d $_{3/2}$) in Figure 4c [46]. The special sp^2 (C-C) bond in the CN from $g\text{-C}_3\text{N}_4$ was

responsible for three peaks in the region of 284 eV in Figure 4d. The existence of the C atom in the aromatic ring linked to NH_x is shown by the peak at 286.5 eV [47]. The N-C=N triazine ring sp^2 hybrid carbon was responsible for the appearance of a strong peak at 282 eV. In Figure 4e, the presence of metal oxide (M-O) bindings such as Ce-O, Nb-O, and O with a hydrocarbon or hydroxyl group (O-C or O-H) are depicted by the two convoluted peaks of O 1s at 531.7 eV and 533.4 eV [40]. The above results confirmed the successful modification of Ce_3NbO_7 over $g\text{-C}_3\text{N}_4$ in NCs.

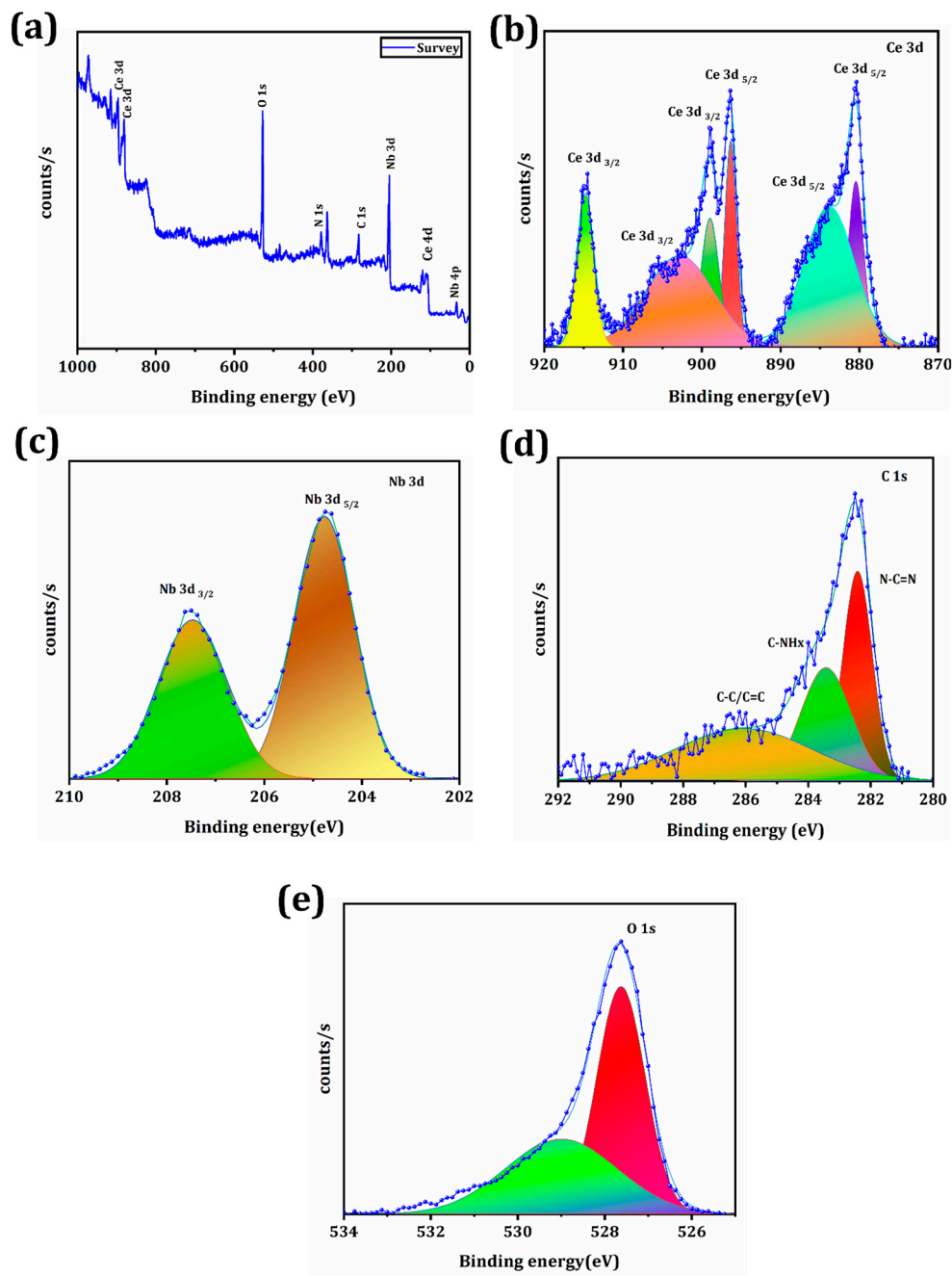


Figure 4. XPS spectra of the $\text{CeO}_2/\text{Ce}_3\text{NbO}_7/g\text{-C}_3\text{N}_4$ NCs. (a) The XPS survival spectrum. (b–e) The core level spectrum of Ce 3d, Nb 3d, C 1s, and O 1 s, respectively.

3.2. Photothermal Performance of $\text{CeO}_2/\text{Ce}_3\text{NbO}_7/g\text{-C}_3\text{N}_4$ NCs

$g\text{-C}_3\text{N}_4$ is a superior photothermal agent due to its rich carbon supply, and it can be easily dispersed in H_2O , is photostable, and is environmentally friendly in nature [48]. The $\text{CeO}_2/\text{Ce}_3\text{NbO}_7/g\text{-C}_3\text{N}_4$ NCs were expected to perform effectively in PTT therapy utilizing

808 nm laser irradiation. Figure 5a shows the time-dependent temperature elevation curve of $\text{CeO}_2/\text{Ce}_3\text{NbO}_7/\text{g-C}_3\text{N}_4$ NCs for various concentrations (0, 0.1, 0.2, 0.5, 1, and 2 mg/mL), which confirms that the temperature is a concentration-dependent one. The heating-cooling curve of the NCs proved that they possess good thermal stability, as presented in Figure 5b. Figure 5c shows the IR images of NCs, demonstrating that the temperature elevation of the NCs has increased over time (0 to 5 min). Furthermore, the NCs PCE (η) was calculated as 49.5%. These results confirm that the prepared NCs have good photothermal stability under NIR irradiation.

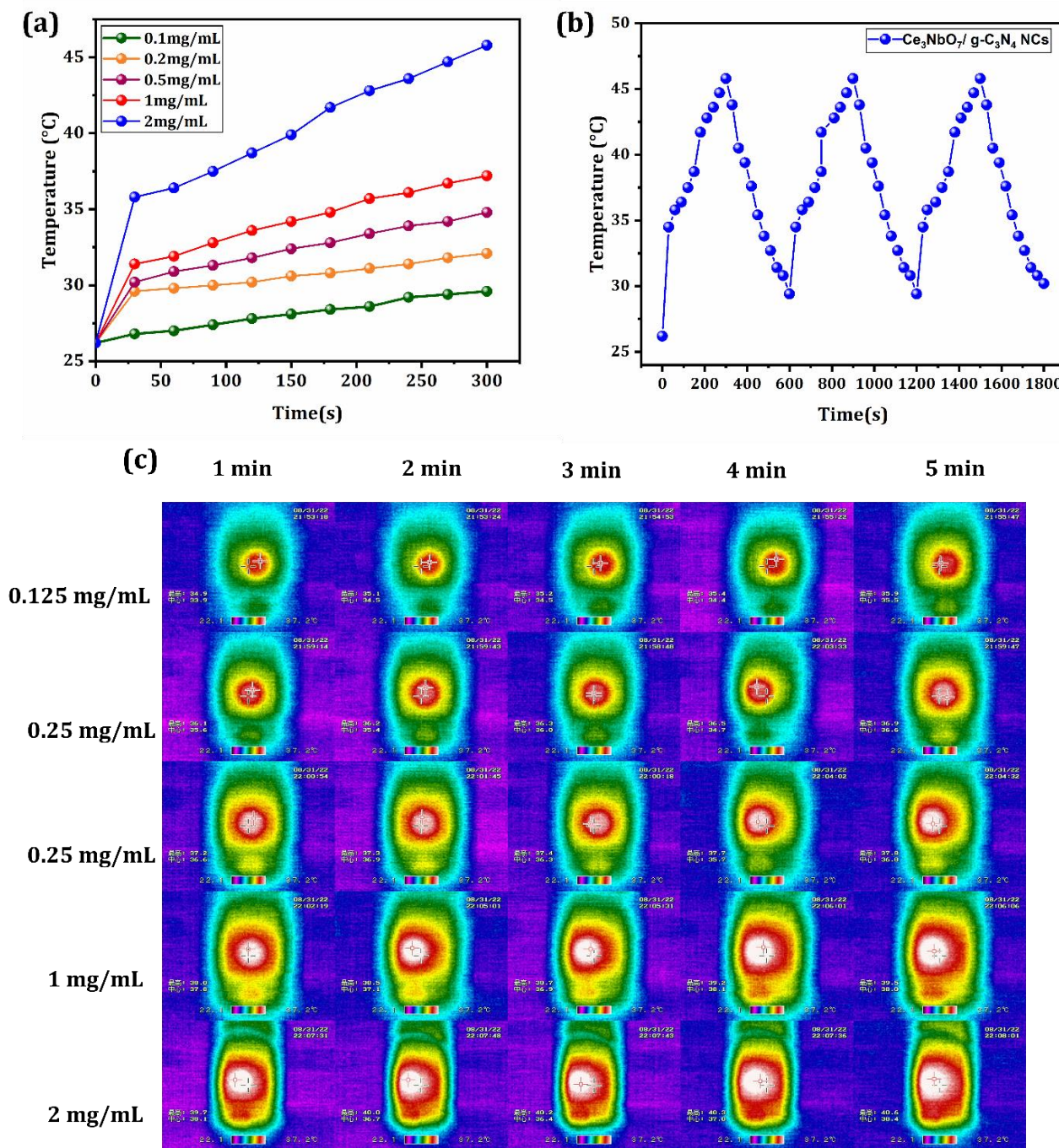


Figure 5. In vitro photothermal responses of the $\text{CeO}_2/\text{Ce}_3\text{NbO}_7/\text{g-C}_3\text{N}_4$ NCs (those Chinese characters in the figure represents the respective temperature range): (a) temperature changes of the $\text{CeO}_2/\text{Ce}_3\text{NbO}_7/\text{g-C}_3\text{N}_4$ NCs aqueous solutions at different concentrations in 1 W/cm². (b) Thermal stability of the synthesized NCs under irradiation with a 1 W/cm² NIR laser source. (c) Infrared thermal images of the NCs at a power density of 1 W/cm².

3.3. Fenton Catalytic Property of the Synthesized $\text{CeO}_2/\text{Ce}_3\text{NbO}_7/g\text{-C}_3\text{N}_4$ NCs

Methylene blue (MB) was employed for the detection and quantification of hydroxyl radical ($\text{OH}\bullet$) to investigate the capacity of $\text{CeO}_2/\text{Ce}_3\text{NbO}_7/g\text{-C}_3\text{N}_4$ NCs to generate $\text{OH}\bullet$ under the circumstances of TME for CDT. Ce mediates the reaction of H_2O_2 to generate $\text{OH}\bullet$ via Fenton-type reactions. Figure 6a depicts the UV-visible curve for MB in water (pH = 7.4) and H_2O_2 (pH = 6.5) solutions, where the absorbance peak was observed at the maximum wavelength of 664.6 nm in room temperature with little changes, indicating MB could not be degraded under various pH conditions. In Figure 6b, the degradation curve of MB with H_2O_2 is given for varying time intervals from 0 to 20 min at 37 °C. Figure 6c presents the MB degradation curve and the calculated amount of synthesized NCs in the absence of laser source for different time durations of 0, 10, 15, and 20 min. Here, the Ce in the NCs actively participates in the Fenton reaction via a cascade mechanism to yield the highly toxic $\text{OH}\bullet$ that rapidly kills cancer cells inside the TME. The degradation efficiency slightly decreased, mainly caused by more Ce^{4+} occupying the H_2O_2 active sites. These results demonstrate that $\text{CeO}_2/\text{Ce}_3\text{NbO}_7/g\text{-C}_3\text{N}_4$ NCs have the best catalytic performance, and they can efficiently catalyze the production of sufficient hydroxyl radicals from H_2O_2 . Figure 6d reveals the photothermally enhanced Fenton reaction. The degradation of MB following exposure to an 808 nm NIR laser was studied to evaluate the impact of the photothermal effect on the Fenton reaction of NCs. It is evident that when the NCs were exposed to an 808 nm NIR laser, MB degradation efficiency increased in the presence of the laser compared to the normal Fenton reaction, supporting the theory that the synthesized NCs firmly control the photothermal enhancement of the Fenton reaction. NCs could generate heat by the photothermal reaction to accelerate the Fenton reaction and the subsequent production of $\text{OH}\bullet$. Additionally, combining photothermal and chemodynamic performance, the prepared NCs act as an optimized therapeutic platform in cancer applications.

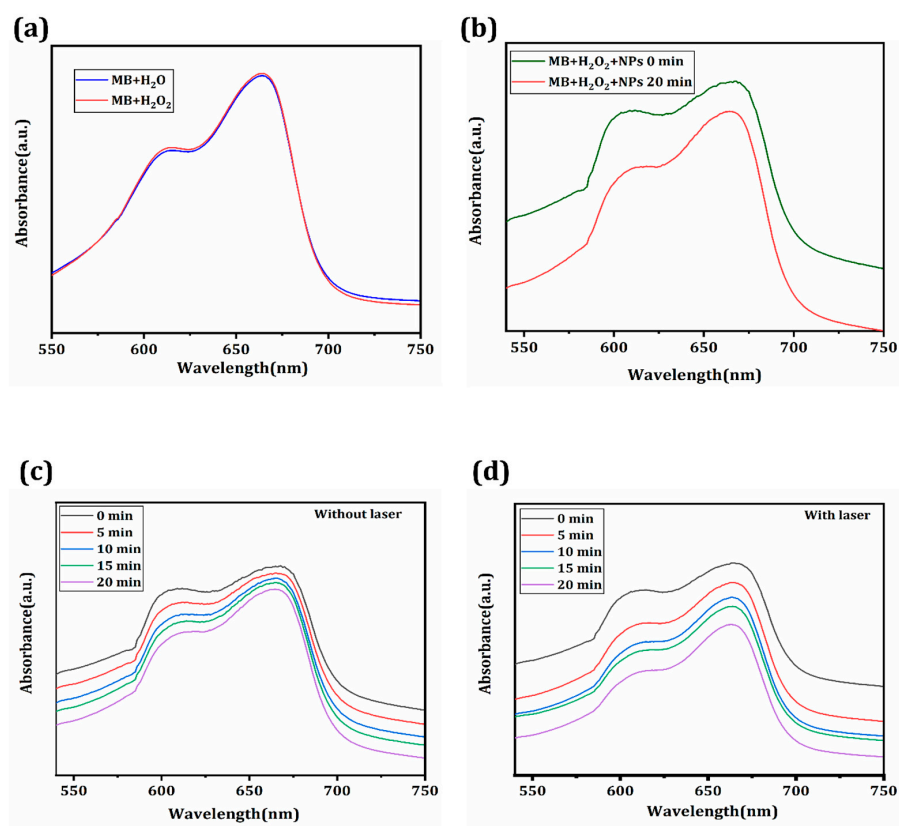


Figure 6. UV-Visible spectra of MB + H_2O and MB + H_2O_2 (a). Degradation plot of MB + $\text{CeO}_2/\text{Ce}_3\text{NbO}_7/g\text{-C}_3\text{N}_4$ NCs at different time intervals (0 and 20 min) (b). The MB degradation of the NCs without laser for different time durations (c). The PTT/CDT of MB degradation efficiency of NCs in the presence of laser (d).

3.4. In Vitro PTT/CDT Performance of $\text{CeO}_2/\text{Ce}_3\text{NbO}_7/\text{g-C}_3\text{N}_4$ NCs towards Liver Cancer

The synergistic therapeutic applications of the NCs were examined using a cell viability assay. Human cancer cells (HepG2) and L929 cells were chosen here to investigate the in vitro cytotoxicity of $\text{CeO}_2/\text{Ce}_3\text{NbO}_7/\text{g-C}_3\text{N}_4$ NCs by utilizing an MTT assay. Designing nanomaterials for various biomedical applications requires careful consideration of biocompatibility. Here, the primary intrinsic cytotoxicity of the $\text{CeO}_2/\text{Ce}_3\text{NbO}_7/\text{g-C}_3\text{N}_4$ NCs of L929 was assessed in Figure 7a, where the cell viability of L929 is high around 93% compared to HepG2 cells. From this, we conclude that NCs are biocompatible. The relative cell viability of HepG2 cells without laser at pH 7.4 was estimated at 84% for the highest concentration of 100 $\mu\text{g/mL}$ of NCs, as shown in Figure 7a. These findings proved that $\text{CeO}_2/\text{Ce}_3\text{NbO}_7/\text{g-C}_3\text{N}_4$ NCs show negligible cytotoxicity compared to other targeting-agent-based biomedical systems, ensuring their eligibility for further therapeutic application in research [49]. The in vitro tumor-cell-killing effectiveness of $\text{CeO}_2/\text{Ce}_3\text{NbO}_7/\text{g-C}_3\text{N}_4$ NCs was assessed after 808 nm laser radiation (1 W/cm²) for 5 min (Figure 7b). After laser radiation, as seen in Figure 7b, $\text{CeO}_2/\text{Ce}_3\text{NbO}_7/\text{g-C}_3\text{N}_4$ NCs significantly increased the concentration-dependent cell death of HepG2 cells. This demonstrated that NCs possess the capacity for benign photothermal cell death. Figure 7c represents the respective cell viability under pH = 6.5 (CDT). The NCs powerfully enhance the production of $\text{OH}\bullet$. Endogenous CDT is made possible without external stimuli owing to the $\text{CeO}_2/\text{Ce}_3\text{NbO}_7/\text{g-C}_3\text{N}_4$ NCs' potent catalysis of H_2O_2 and dissociation to create $\text{OH}\bullet$. Because of their metabolism, cancer cells inside the TME typically create H_2O_2 naturally. Additionally, the effectiveness of $\text{CeO}_2/\text{Ce}_3\text{NbO}_7/\text{g-C}_3\text{N}_4$ NCs against the HepG2 cells in the tumor environment (pH = 6.5) was further evaluated. The HepG2 cell viability marginally decreased without laser irradiation when the $\text{CeO}_2/\text{Ce}_3\text{NbO}_7/\text{g-C}_3\text{N}_4$ NCs concentration increased. In order to kill cancer cells, $\text{CeO}_2/\text{Ce}_3\text{NbO}_7/\text{g-C}_3\text{N}_4$ NCs can catalyze H_2O_2 dissociation to produce toxic $\text{OH}\bullet$ (Figure 7c). The reduction in cell viability was more significant when CDT and PTT (an 808 nm laser) were coupled. Approximately 68% of HepG2 cells were destroyed at a concentration of 100 $\mu\text{g/mL}$ of $\text{CeO}_2/\text{Ce}_3\text{NbO}_7/\text{g-C}_3\text{N}_4$ NCs (Figure 7c). Overall, MTT cell viability results suggested that the PTT could enhance CDT efficacy, leading to a synergistic effect in the ablation of cancer cells by combination therapy.

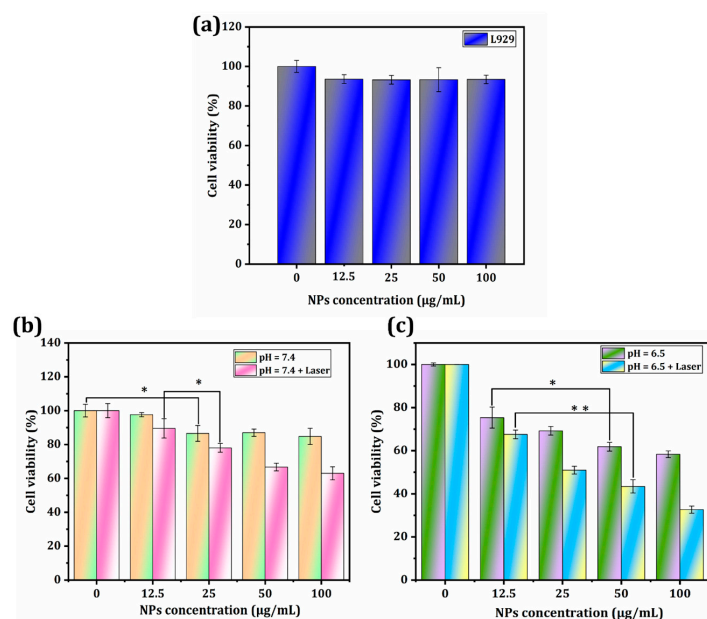


Figure 7. In vitro cytotoxicity analysis of L929 cells (a); synergistic therapeutic application of $\text{CeO}_2/\text{Ce}_3\text{NbO}_7/\text{g-C}_3\text{N}_4$ NCs towards HepG2 cells with the incorporation of 808 nm of NIR laser at pH = 7.4 (b); cytotoxicity analysis of the $\text{CeO}_2/\text{Ce}_3\text{NbO}_7/\text{g-C}_3\text{N}_4$ NCs + laser at pH = 6.5 (c). Statistical analysis (*, **) was performed by student's *t*-test method.

4. Discussion

We propose a distinctive perspective on conjugated g-C₃N₄ with CeO₂/Ce₃NbO₇ hollow spheres to form CeO₂/Ce₃NbO₇/g-C₃N₄ NCs. g-C₃N₄ exhibits excellent NIR absorption rates, which suggests they have a strong potential for PTT applications. CeO₂/Ce₃NbO₇/g-C₃N₄ NCs (2.0 mg/mL) increased in temperature after 300 s. Under 808nm of laser irradiation exposure, CeO₂/Ce₃NbO₇/g-C₃N₄ NCs displayed an excellent photothermal conversion efficiency (η) of around 49.5% and better thermal stability after three consecutive cycles.

Ce³⁺ in the NCs actively participates in the Fenton mechanism to yield the reactive oxygen species (OH•) that drastically kills the tumor cells inside the TME. Here, the MB degradation plot provides clear evidence for the production of OH• radicals with and without a laser source. From those results, we confirm that the NCs show the best catalytic performance along with laser (808 nm) in cancer theranostics.

Furthermore, concentration-dependent cell death occurs due to the PTT/CDT effect in CeO₂/Ce₃NbO₇/g-C₃N₄ NCs. Compared to PTT and CDT, the in vitro studies convey that the synergistic PTT/CDT exhibits decreased cell survival of 30% HepG2 cells for (100 mg/mL) NCs. The excellent cell-killing ability is mainly due to the dual therapeutic performance of NCs toward cancer cells. Based on these results, the synthesized NCs hold great potency in both PTT and CDT for ablating cancer cells, and are biocompatible.

5. Conclusions

Herein, we developed a CeO₂/Ce₃NbO₇ hollow sphere modified with graphitic carbon nitride (g-C₃N₄) to create a synergistic therapeutic application using CDT and PTT for cancer treatment. Moreover, the cerium niobate hollow spheres were prepared by a facile hydrothermal method for cancer theranostics, and the NCs showed outstanding photothermal conversion efficiency (η) of 49.5% due to the presence of g-C₃N₄. Under laser irradiation, it not only ablates the tumor cells but also enhances the Fenton reaction, boosting the conversion of Ce³⁺ to Ce²⁺ to generate ROS and showing excellent photothermal behavior. In vitro, studies demonstrated the excellent ability for cell apoptosis of tumor cells using synergistic therapeutic modes. The current research can assist in developing novel materials and various photothermal agents for multifunctional therapeutic applications in cancer treatment. As a result of our study, novel nanoplatforms can be created for the precise and highly efficient treatment of liver tumors.

Author Contributions: K.S.M.: Writing—original draft, methodology, formal analysis, data curation, visualization, writing—review and editing. S.T.: Writing—review and editing, methodology, formal analysis, data curation, visualization. Y.-C.L.: Writing—review and editing, methodology, formal analysis, data curation, visualization. R.S.: Investigation, formal analysis, data curation. U.D.: Writing—review and editing, methodology, formal analysis, data curation, visualization. A.-N.W.: Resources. M.H.: Resources. R.-J.C.: Conceptualization, methodology, supervision, project administration, funding acquisition, writing—review and editing. All authors have read and agreed to the published version of the manuscript.

Funding: The authors are grateful for the financial support provided by the Ministry of Science and Technology of Taiwan (MOST 108-2628-E-027-003-MY3; MOST 111-2221-E-027-105).

Data Availability Statement: The data presented in this study are available upon request from the corresponding author.

Acknowledgments: Technical assistance from the Precision Analysis and Material Research Center of National Taipei University of Technology (Taipei Tech) is appreciated.

Conflicts of Interest: The authors declare no conflict of interest.

References

1. Deng, Z.; Fang, C.; Ma, X.; Li, X.; Zeng, Y.-J.; Peng, X. One stone two birds: Zr-Fc metal–organic framework nanosheet for synergistic photothermal and chemodynamic cancer therapy. *ACS Appl. Mater. Interfaces* **2020**, *12*, 20321–20330. [[CrossRef](#)]
2. Bray, F.; Ferlay, J.; Soerjomataram, I.; Siegel, R.L.; Torre, L.A.; Jemal, A. Global cancer statistics 2018: GLOBOCAN estimates of incidence and mortality worldwide for 36 cancers in 185 countries. *CA A Cancer J. Clin.* **2018**, *68*, 394–424. [[CrossRef](#)]

3. Weiderpass, E. Lifestyle and cancer risk. *J. Prev. Med. Public Health* **2010**, *43*, 459–471. [[CrossRef](#)]
4. Chen, Y.C.; Hunter, D.J. Molecular epidemiology of cancer. *CA A Cancer J. Clin.* **2005**, *55*, 45–54. [[CrossRef](#)]
5. Arico, M.; Schrappe, M.; Hunger, S.P.; Carroll, W.L.; Conter, V.; Galimberti, S.; Manabe, A.; Saha, V.; Baruchel, A.; Vettenranta, K. Clinical outcome of children with newly diagnosed Philadelphia chromosome-positive acute lymphoblastic leukemia treated between 1995 and 2005. *J. Clin. Oncol.* **2010**, *28*, 4755. [[CrossRef](#)] [[PubMed](#)]
6. Monsalve, J.; Kapur, J.; Malkin, D.; Babyn, P.S. Imaging of cancer predisposition syndromes in children. *Radiographics* **2011**, *31*, 263–280. [[CrossRef](#)] [[PubMed](#)]
7. Center, M.M.; Jemal, A. International Trends in Liver Cancer Incidence Rates International Liver Cancer Incidence Trends. *Cancer Epidemiol. Biomark. Prev.* **2011**, *20*, 2362–2368. [[CrossRef](#)]
8. Siegel, R.L.; Miller, K.D.; Jemal, A. Cancer statistics, 2019. *CA A Cancer J. Clin.* **2019**, *69*, 7–34. [[CrossRef](#)] [[PubMed](#)]
9. Anwanwan, D.; Singh, S.K.; Singh, S.; Saikam, V.; Singh, R. Challenges in liver cancer and possible treatment approaches. *Biochim. Et Biophys. Acta (BBA)-Rev. Cancer* **2020**, *1873*, 188314. [[CrossRef](#)]
10. Pérez-López, A.; Martín-Sabroso, C.; Gómez-Lázaro, L.; Torres-Suárez, A.I.; Aparicio-Blanco, J. Embolization therapy with microspheres for the treatment of liver cancer: State-of-the-art of clinical translation. *Acta Biomater.* **2022**, *149*, 1–15. [[CrossRef](#)] [[PubMed](#)]
11. World Health Organization. *International Agency for Research on Cancer Cancer Today*; World Health Organization: Geneva, Switzerland, 2016.
12. Sung, H.; Ferlay, J.; Siegel, R.L.; Laversanne, M.; Soerjomataram, I.; Jemal, A.; Bray, F. Global cancer statistics 2020: GLOBOCAN estimates of incidence and mortality worldwide for 36 cancers in 185 countries. *CA A Cancer J. Clin.* **2021**, *71*, 209–249. [[CrossRef](#)]
13. Starley, B.Q.; Calcagno, C.J.; Harrison, S.A. Nonalcoholic fatty liver disease and hepatocellular carcinoma: A weighty connection. *Hepatology* **2010**, *51*, 1820–1832. [[CrossRef](#)]
14. Feng, M.; Pan, Y.; Kong, R.; Shu, S. Therapy of primary liver cancer. *Innovation* **2020**, *1*, 100032. [[CrossRef](#)] [[PubMed](#)]
15. Wang, Z.; Yu, W.; Yu, N.; Li, X.; Feng, Y.; Geng, P.; Wen, M.; Li, M.; Zhang, H.; Chen, Z. Construction of CuS@ Fe-MOF nanoplatfoms for MRI-guided synergistic photothermal-chemo therapy of tumors. *Chem. Eng. J.* **2020**, *400*, 125877. [[CrossRef](#)]
16. Fan, W.; Yung, B.; Huang, P.; Chen, X. Nanotechnology for multimodal synergistic cancer therapy. *Chem. Rev.* **2017**, *117*, 13566–13638. [[CrossRef](#)]
17. Liu, Y.; Bhattarai, P.; Dai, Z.; Chen, X. Photothermal therapy and photoacoustic imaging via nanotheranostics in fighting cancer. *Chem. Soc. Rev.* **2019**, *48*, 2053–2108. [[CrossRef](#)]
18. Zhu, P.; Chen, Y.; Shi, J. Nanoenzyme-augmented cancer sonodynamic therapy by catalytic tumor oxygenation. *ACS Nano* **2018**, *12*, 3780–3795. [[CrossRef](#)]
19. Cheng, L.; Wang, C.; Feng, L.; Yang, K.; Liu, Z. Functional nanomaterials for phototherapies of cancer. *Chem. Rev.* **2014**, *114*, 10869–10939. [[CrossRef](#)] [[PubMed](#)]
20. Tang, Z.; Liu, Y.; He, M.; Bu, W. Chemodynamic therapy: Tumour microenvironment-mediated Fenton and Fenton-like reactions. *Angew. Chem.* **2019**, *131*, 958–968. [[CrossRef](#)]
21. Jiang, F.; Ding, B.; Liang, S.; Zhao, Y.; Cheng, Z.; Xing, B.; Lin, J. Intelligent MoS₂-CuO heterostructures with multiplexed imaging and remarkably enhanced antitumor efficacy via synergetic photothermal therapy/chemodynamic therapy/immunotherapy. *Biomaterials* **2021**, *268*, 120545. [[CrossRef](#)]
22. Ng, C.W.; Li, J.; Pu, K. Recent progresses in phototherapy-synergized cancer immunotherapy. *Adv. Funct. Mater.* **2018**, *28*, 1804688. [[CrossRef](#)]
23. Wang, C.; Xu, L.; Liang, C.; Xiang, J.; Peng, R.; Liu, Z. Immunological responses triggered by photothermal therapy with carbon nanotubes in combination with anti-CTLA-4 therapy to inhibit cancer metastasis. *Adv. Mater.* **2014**, *26*, 8154–8162. [[CrossRef](#)]
24. Wu, C.; Wang, S.; Zhao, J.; Liu, Y.; Zheng, Y.; Luo, Y.; Ye, C.; Huang, M.; Chen, H. Biodegradable Fe (III)@ WS₂-PVP nanocapsules for redox reaction and TME-enhanced nanocatalytic, photothermal, and chemotherapy. *Adv. Funct. Mater.* **2019**, *29*, 1901722. [[CrossRef](#)]
25. Liu, Y.; Zhen, W.; Jin, L.; Zhang, S.; Sun, G.; Zhang, T.; Xu, X.; Song, S.; Wang, Y.; Liu, J. All-in-one theranostic nanoagent with enhanced reactive oxygen species generation and modulating tumor microenvironment ability for effective tumor eradication. *ACS Nano* **2018**, *12*, 4886–4893. [[CrossRef](#)]
26. Wan, S.-S.; Cheng, Q.; Zeng, X.; Zhang, X.-Z. A Mn (III)-sealed metal-organic framework nanosystem for redox-unlocked tumor theranostics. *ACS Nano* **2019**, *13*, 6561–6571. [[CrossRef](#)]
27. Ding, B.; Shao, S.; Jiang, F.; Dang, P.; Sun, C.; Huang, S.; Ma, P.a.; Jin, D.; Kheraif, A.A.A.; Lin, J. MnO₂-disguised upconversion hybrid nanocomposite: An ideal architecture for tumor microenvironment-triggered UCL/MR bioimaging and enhanced chemodynamic therapy. *Chem. Mater.* **2019**, *31*, 2651–2660. [[CrossRef](#)]
28. Gao, S.; Jin, Y.; Ge, K.; Li, Z.; Liu, H.; Dai, X.; Zhang, Y.; Chen, S.; Liang, X.; Zhang, J. Self-supply of O₂ and H₂O₂ by a Nanocatalytic medicine to enhance combined chemo/Chemodynamic therapy. *Adv. Sci.* **2019**, *6*, 1902137. [[CrossRef](#)]
29. Liu, Y.; Jia, Q.; Guo, Q.; Wei, W.; Zhou, J. Simultaneously activating highly selective ratiometric MRI and synergistic therapy in response to intratumoral oxidability and acidity. *Biomaterials* **2018**, *180*, 104–116. [[CrossRef](#)]
30. Duan, L.-Y.; Wang, Y.-J.; Liu, J.-W.; Wang, Y.-M.; Li, N.; Jiang, J.-H. Tumor-selective catalytic nanosystem for activatable theranostics. *Chem. Commun.* **2018**, *54*, 8214–8217. [[CrossRef](#)] [[PubMed](#)]

31. Park, J.; Lim, D.-H.; Lim, H.-J.; Kwon, T.; Choi, J.-s.; Jeong, S.; Choi, I.-H.; Cheon, J. Size dependent macrophage responses and toxicological effects of Ag nanoparticles. *Chem. Commun.* **2011**, *47*, 4382–4384. [[CrossRef](#)]
32. Hu, R.; Fang, Y.; Huo, M.; Yao, H.; Wang, C.; Chen, Y.; Wu, R. Ultrasmall Cu₂-xS nanodots as photothermal-enhanced Fenton nanocatalysts for synergistic tumor therapy at NIR-II biowindow. *Biomaterials* **2019**, *206*, 101–114. [[CrossRef](#)]
33. Wang, Z.; Liu, B.; Sun, Q.; Dong, S.; Kuang, Y.; Dong, Y.; He, F.; Gai, S.; Yang, P. Fusiform-like copper (II)-based metal–organic framework through relief hypoxia and GSH-depletion co-enhanced starvation and chemodynamic synergetic cancer therapy. *ACS Appl. Mater. Interfaces* **2020**, *12*, 17254–17267. [[CrossRef](#)] [[PubMed](#)]
34. Feng, N.; Liu, Y.; Dai, X.; Wang, Y.; Guo, Q.; Li, Q. Advanced applications of cerium oxide based nanozymes in cancer. *RSC Adv.* **2022**, *12*, 1486–1493. [[CrossRef](#)]
35. Asati, A.; Santra, S.; Kaittanis, C.; Nath, S.; Perez, J.M. Oxidase-like activity of polymer-coated cerium oxide nanoparticles. *Angew. Chem.* **2009**, *121*, 2344–2348. [[CrossRef](#)]
36. Gao, Y.; Chen, K.; Ma, J.-l.; Gao, F. Cerium oxide nanoparticles in cancer. *OncoTargets Ther.* **2014**, *7*, 835–840. [[CrossRef](#)]
37. Song, X.; Chen, Q.; Liu, Z. Recent advances in the development of organic photothermal nano-agents. *Nano Res.* **2015**, *8*, 340–354. [[CrossRef](#)]
38. Liao, G.; He, F.; Li, Q.; Zhong, L.; Zhao, R.; Che, H.; Gao, H.; Fang, B. Emerging graphitic carbon nitride-based materials for biomedical applications. *Prog. Mater. Sci.* **2020**, *112*, 100666. [[CrossRef](#)]
39. Bosio, G.N.; Mártire, D.O. Carbon nitride nanomaterials with application in photothermal and photodynamic therapies. *Photodiagnosis Photodyn. Ther.* **2022**, *37*, 102683. [[CrossRef](#)]
40. Liu, X.; Tseng, C.-L.; Lin, L.-Y.; Lee, C.-A.; Li, J.; Feng, L.; Song, L.; Li, X.; He, J.-H.; Sakthivel, R. Template-free synthesis of mesoporous Ce₃NbO₇/CeO₂ hollow nanospheres for label-free electrochemical immunosensing of leptin. *Sens. Actuators B Chem.* **2021**, *341*, 130005. [[CrossRef](#)]
41. Sanjay, B.P.; Swamy, N.K.; Yashas, S.R.; Sandeep, S. Design of an electrochemical sensor using 2D sheet-like Cu@ g-C₃N₄ transducer matrix for electroanalysis of catechol. *J. Electrochem. Soc.* **2021**, *168*, 076511. [[CrossRef](#)]
42. Guoguang, Z.; Qin, L.; Qianfeng, F. Structure and Dielectric Study of Ce₃NbO₇. *J. Rare Earths* **2007**, *25*, 730–733. [[CrossRef](#)]
43. Farahmandjou, M.; Zarinkamar, M.; Firoozabadi, T. Synthesis of Cerium Oxide (CeO₂) nanoparticles using simple CO-precipitation method. *Rev. Mex. De Física* **2016**, *62*, 496–499.
44. Feng, L.; He, F.; Yang, G.; Gai, S.; Dai, Y.; Li, C.; Yang, P. NIR-driven graphitic-phase carbon nitride nanosheets for efficient bioimaging and photodynamic therapy. *J. Mater. Chem. B* **2016**, *4*, 8000–8008. [[CrossRef](#)]
45. Sakthivel, R.; Annalakshmi, M.; Chen, S.-M.; Kubendhiran, S.; Anbazhagan, R.; Tsai, H.-C. A novel sensitive and reliable electrochemical determination of palmatine based on CeO₂/RGO/MWCNT ternary composite. *J. Taiwan Inst. Chem. Eng.* **2019**, *96*, 549–558. [[CrossRef](#)]
46. Liu, F.; Wang, Y.; Kong, X.; Lei, D.; Zhang, F.; Lei, X. A hierarchical Nb₂O₅@ NiFe-MMO rod array, fabricated and used as a structured photocatalyst. *RSC Adv.* **2019**, *9*, 6177–6183. [[CrossRef](#)]
47. Baranowska, D.; Kędzierski, T.; Aleksandrak, M.; Mijowska, E.; Zielińska, B. Influence of hydrogenation on morphology, chemical structure and photocatalytic efficiency of graphitic carbon nitride. *Int. J. Mol. Sci.* **2021**, *22*, 13096. [[CrossRef](#)] [[PubMed](#)]
48. Yan, S.; Li, Z.; Zou, Z. Photodegradation performance of g-C₃N₄ fabricated by directly heating melamine. *Langmuir* **2009**, *25*, 10397–10401. [[CrossRef](#)]
49. Zhang, L.; Jiang, H.; Selke, M.; Wang, X. Selective cytotoxicity effect of cerium oxide nanoparticles under UV irradiation. *J. Biomed. Nanotechnol.* **2014**, *10*, 278–286. [[CrossRef](#)] [[PubMed](#)]

Disclaimer/Publisher’s Note: The statements, opinions and data contained in all publications are solely those of the individual author(s) and contributor(s) and not of MDPI and/or the editor(s). MDPI and/or the editor(s) disclaim responsibility for any injury to people or property resulting from any ideas, methods, instructions or products referred to in the content.